AIAA JOURNAL
Vol. 39, No. 11, November 2001

Shock-Wave/Turbulent Boundary-Layer Interactions in Nonequilibrium Flows

Francesco Grasso*
University of Rome "La Sapienza," 00184 Rome, Italy
Marco Marini†
Centro Italiano Ricerche Aerospaziali, 81043 Capua, Italy
Giuliano Ranuzzi‡ and Simone Cuttica‡
University of Rome "La Sapienza," 00184 Rome, Italy
and
Bruno Chanetz§
ONERA, 92190 Meudon, France

Shock-wave/turbulent boundary-layer interactions in the presence of thermal and chemical nonequilibrium phenomena are analyzed. The approach relies on a linear eddy viscosity two-equation turbulence modeling that accounts for the coupling of turbulence with chemistry and vibration, and it employs a total variation diminishing finite volume numerical methodology. The capability of the model has first been assessed for a cylinder flare configuration, and results have been compared with experiments. The model has then been applied to assess the aerodynamic performance of control surfaces of a reusable launch vehicle. In particular, the effects of wall temperature and flap deflection on the separation, aerothermal loads, and flap efficiency have been studied. The analysis shows that turbulence becomes important for flap deflection angles greater than a critical value [$\mathcal{O}$ (15 deg)], thus avoiding the crisis of the flap efficiency that is observed under laminar conditions and extending the operating capabilities of the control surface. The study also shows that the wall temperature affects significantly the efficiency and the operating envelope of the flap primarily under turbulent conditions.

Introduction

SHOCK-WAVE/boundary-layer interactions in high-speed flows have a large impact on the design of hypersonic vehicles for the presence of extended recirculation regions and intense local heating. Indeed, the occurrence of such interactions may deteriorate the aerodynamic efficiency of the control surfaces, making critical the flight control and the structural integrity of the vehicle.[1] In particular, the position of primary separation has the greatest importance in determining the location of the shock configuration that affects the aerodynamic quantities. The complexity of the phenomenon and its importance in the design of aerodynamic shape and thermal protection system of a hypersonic vehicle require the understanding of the controlling effects and their quantitative characterization.

In the past few decades several studies dealing with the shock-wave/boundary-layer interaction phenomena were conducted, either for laminar or turbulent conditions, mainly for cold hypersonic flows, that is, for low enthalpy. Extensive reviews describing the physical phenomena of shock-wave/boundary-layer interaction in hypersonic regime and some correlation laws for incipient separation conditions, characteristic pressures, separation extent, and peak heating can be found in the works of Needham and Stollery,[2] Holden,[3] and Delery.[4] Experimental studies of both laminar and turbulent shock-wave/boundary-layer interactions from supersonic through hypersonic regime were conducted by Holden,[3] who has investigated the effects of Mach and Reynolds numbers, ramp angle, and leading-edge bluntness on the flowfield in terms of upstream influence, separation extent, and peak heating. In Ref. 3 it was established that upstream influence increases with ramp angle and decreases with Mach number, and it is affected also by the Reynolds number (only weakly in a fully turbulent regime), whereas bluntness reduces pressure and thermal loads because the interaction for a blunt leading edge occurs in (a locally) supersonic regime. Delery[4] has experimentally shown that upstream influence and separation length increase with ramp angle for a given Mach and Reynolds number and decrease with Mach number for a given ramp angle and Reynolds number. In Ref. 4 it was also shown that the main flow features remain similar in laminar and turbulent conditions, the differences being the extent of the interaction, that is, the characteristic scale, and the pressure and thermal loads. Grasso and Marini[5] have studied hypersonic viscous flows dominated by strong shock-wave/laminar boundary-layer interactions over wing–flap and wing–fuselage junction configurations and have assessed the effects of the control surface deflection angle, leading-edge shape, and viscous interaction parameter. Scaling laws for the upstream influence, peak heating, and aerodynamic coefficients have been established by means of numerical simulations and theoretical considerations. Grasso et al.[6] have characterized the different controlling mechanisms of the shock-wave/boundary-layer interaction phenomena and have critically reviewed the various correlation formulas (skin friction, Stanton number, characteristic pressures, and peak heating) applicable in the different regions.

Under reentry conditions, the gas may not always be treated as an ideal gas, and real gas effects such as vibrational excitation and chemical reactions affect significantly such phenomena; their influence (and coupling with turbulence) must be necessarily accounted for. Grasso and Leone[7] have studied the influence of chemical reactions under the assumption of thermal and chemical equilibrium for shock-wave/laminar boundary-layer interactions over compression ramps. In Ref. 7 it is shown that due to dissociation reactions (in equilibrium) the temperature is lowered and the shock waves are weakened, as well as their interaction with the boundary layer. The results of Ref. 7 show a reduction of the separation extent due to real gas effects; however, the peak heating (on the ramp) still correlates with the inviscid pressure jump across the shock. Recently, Mallinson et al.[8] have conducted high-enthalpy compression

Received 14 April 2000; revision received 1 April 2001; accepted for publication 8 May 2001.

*Professor, Department of Mechanics and Aeronautics, Via Eudossiana 18. Associate Fellow AIAA.
†Research Scientist, Aerothermodynamics Laboratory, Via Maiorise.
‡Aeronautical Engineer, Department of Mechanics and Aeronautics, Via Eudossiana 18.
§Head of Hypersonic Project, Fundamental and Experimental Aerodynamic Department, Rue des Vertugadins.

ramp flow experiments at various stagnation conditions and ramp angles, concluding that real gas effects on the pressure distribution, incipient separation angle, and peak heating are negligible, at least for the conditions they have examined. In Ref. 9 it has also been shown that typical correlation laws for shock-wave/boundary-layer interactions, originally derived for ideal gas flows, are still valid when the boundary layer is chemically frozen provided local correlating parameters are properly defined. Krek et al.[10] have observed a reduction of the separation extent with stagnation enthalpy at a constant viscous interaction parameter for a hyperboloid flare model in the DLR High Enthalpy Göttingen (HEG) shock tunnel, whereas Davis[11] has not observed this behavior on the HALIS axisymmetric configuration in the T5 Hypervelocity Shock Tunnel at the California Institute of Technology. Further numerical studies on the interaction of a shock impinging on a flat plate[12] have shown that dissociation reactions reduce the interaction extent. This is mainly due to a reduction of the pressure behind the reattachment shock in the presence of negligible dissociation upstream of reattachment. Davis and Sturtevant[13] have investigated experimentally and theoretically nonequilibrium effects on separation length using a double-wedge geometry and nitrogen test gas. Those authors have concluded that, for weak shock strength, dissociation reactions outside of the boundary layer may yield a reduction of separation length depending on the freestream dissociation; likewise, recombination reactions within the boundary layer and upstream of separation are responsible for a slight decrease of separation length (with respect to a nonreacting boundary layer). In addition, in Ref. 13 it is shown that at high enthalpy the separation extent increases due to recombination in the free-shear layer downstream of separation (mainly because of the combined effects of freestream dissociation and a cold wall).

The objective of the present work is to assess the influence of turbulence in the presence of thermal and chemical nonequilibrium phenomena on shock-wave/boundary-layer interactions that occur around the control surfaces of a reusable launch vehicle. In particular, a model is developed that assumes 1) a single translational temperature to characterize the translational and rotational modes, 2) a single vibrational temperature for vibrational excitation of the diatomic species that are assumed to behave as harmonic oscillators; 3) finite-rate chemistry for nonionizing air, and 4) a gradient-law assumption to account for the turbulent transport of momentum, energy (translational, rotational, and vibrational) and species partial masses. The methodology relies on a linear eddy viscosity two-equation (K–ε) model that accounts for the coupling of turbulence with chemistry and vibration through properly defined turbulent Prandtl numbers, and it employs a numerical scheme based on a finite volume total variation diminishing approach with a point-implicit treatment of the source terms.

The model is first applied to a hypersonic flow over an axisymmetric cylinder flare configuration at ONERA-F4 high-enthalpy wind-tunnel conditions, the goal being the validation of the methodology through comparison with available experimental data. The model is then applied to analyze shock-wave/boundary-layer interaction phenomena occurring over the body-flap of the Future European System Transportation Investigation Program (FESTIP) FSSC-15-OAE suborbital hopper vehicle in flight conditions. In particular, we have studied the influence of the wall temperature and the body-flap deflection on the separation characteristics, on the aerothermal loads, and on the aerodynamic efficiency of the flap.

In the following sections the physical model and the numerical approach are developed, the test cases are described, the computational results are discussed, and conclusions are given.

Governing Equations

In the present work, we have developed a model for the analysis of shock-wave/turbulent boundary-layer interactions; the model relies on the Reynolds-averaged formulation of the conservation laws of a mixture of gases in vibrational and chemical nonequilibrium. As commonly done in the case of compressible turbulent flows of an ideal gas, the governing equations have been formulated by introducing both Favre and conventional time averages. In particular, the Favre average $\tilde{(\ )}$ is adopted for the species mass fraction Y_k and molar fraction X_k, the energy (total E and vibrational e_V), and the velocity field u_i, whereas the time average $\bar{(\ )}$ is employed for the pressure p and the total density ρ. In differential form the equations are

$$\frac{\partial}{\partial t}(\bar{\rho}\tilde{Y}_k) + \frac{\partial}{\partial x_j}(\bar{\rho}\tilde{Y}_k\tilde{u}_j) = -\frac{\partial}{\partial x_j}(J_{k,j} + \bar{\rho}\widetilde{u_j''Y_k''}) + \bar{\omega}_k \qquad k = 1, 5$$

$$\frac{\partial}{\partial t}(\bar{\rho}\tilde{u}_i) + \frac{\partial}{\partial x_j}(\bar{\rho}\tilde{u}_i\tilde{u}_j) = -\frac{\partial}{\partial x_j}(\bar{p}\delta_{ij} - \sigma_{ij} + \bar{\rho}\widetilde{u_i''u_j''})$$

$$\frac{\partial}{\partial t}(\bar{\rho}\tilde{E}) + \frac{\partial}{\partial x_j}\left[\bar{\rho}\tilde{u}_j\left(\tilde{E} + \frac{\bar{p}}{\bar{\rho}}\right)\right] = \frac{\partial}{\partial x_j}(\tilde{u}_i\sigma_{ij} - q_j - \bar{\rho}\tilde{u}_j\widetilde{u_i''u_j''} - \bar{\rho}\widetilde{u_j''e_T''} - \bar{\rho}\widetilde{u_j''e_V''})$$

$$\frac{\partial}{\partial t}(\bar{\rho}\tilde{e}_V) + \frac{\partial}{\partial x_j}(\bar{\rho}\tilde{e}_V\tilde{u}_j) = -\frac{\partial}{\partial x_j}(q_{V,j} + \bar{\rho}\widetilde{u_j''e_V''}) + \bar{S}_V \tag{1}$$

where

$$\sigma_{ij} = 2\mu\bar{S}_{ij} - \frac{2}{3}\mu\bar{S}_{ll}\delta_{ij}, \qquad J_{k,j} = -\bar{\rho}D_k\frac{\partial\tilde{X}_k}{\partial x_j}$$

$$q_j = -(\eta_{\mathrm{tr}} + \eta_{\mathrm{rot}})\frac{\partial\tilde{T}}{\partial x_j} - \eta_V\frac{\partial\tilde{T}_V}{\partial x_j} - \sum_k \bar{\rho}\tilde{h}_k D_k\frac{\partial\tilde{X}_k}{\partial x_j}$$

$$q_{V,j} = -\eta_V\frac{\partial\tilde{T}_V}{\partial x_j} - \sum_m \bar{\rho}\tilde{h}_{m_V} D_m\frac{\partial\tilde{X}_m}{\partial x_j}$$

$$\tilde{E} = \tilde{e}_T + \tilde{e}_V + \sum_k \tilde{Y}_k\,\Delta h_k^0 + \frac{1}{2}\tilde{u}_i\tilde{u}_i + \sum_k \widetilde{Y_k''e_{k_T}''} + \sum_m \widetilde{Y_m''e_{m_V}''} + K \tag{2}$$

$\bar{S}_{ij} = 1/2(\partial\bar{u}_i/\partial x_j + \partial\bar{u}_j/\partial x_i)$ is the symmetric part of the mean strain tensor, and $\bar{\omega}_k$ and Δh_k^0 are, respectively, the average reaction rate production and the enthalpy of formation of species k; in addition, subscript m refers to molecular species.

The Favre-averaged internal energy (of the mixture) contributions that depend, respectively, on the translational and vibrational temperatures are

$$\tilde{e}_T = \sum_k \tilde{Y}_k\tilde{e}_{k_T}, \qquad \tilde{e}_V = \sum_m \tilde{Y}_m\tilde{e}_{m_V}$$

and $K = \widetilde{u_i''u_i''}/2$ is the turbulent kinetic energy. The molecular mixture viscosity μ, the thermal conductivity coefficients, η_{tr}, η_{rot} and η_V, and the diffusion coefficients of species k in the mixture, D_k, are determined as described in Refs. 14 and 15. The mean pressure $\bar{p}$ is determined from the equation of state, that is,

$$\bar{p} = \bar{\rho}\sum_k R_k(\tilde{Y}_k\tilde{T} + \widetilde{Y_k''T''})$$

The internal energy e_k and the enthalpy h_k of species k are obtained assuming energy modes separability.[15]

For atomic species (and dropping $^-$ and $^\sim$, unless confusion arises) one has

$$e_k = \tfrac{3}{2}R_k\,T + \Delta h_k^0 = e_{k_T} + \Delta h_k^0 \tag{3}$$

whereas for diatomic species one obtains

$$e_m = \tfrac{5}{2}R_m\,T + e_{m_V} + \Delta h_m^0 = e_{m_T} + e_{m_V} + \Delta h_m^0 \tag{4}$$

and the vibrational energy contribution is obtained assuming Boltzmann distribution at the vibrational temperature T_V, thus yielding

$$e_{m_V} = R_m \theta_m^V \left\{ 1 \Big/ \left[\exp\left(\theta_m^V \Big/ T_V\right) - 1 \right] \right\} \tag{5}$$

where θ_m^V is the characteristic vibrational temperature.[16] The reaction rate productions have been determined assuming the 17-reaction mechanism of Ref. 16, whereby the coupling between vibration and dissociation has been taken into account by introducing a reaction-rate-controlling temperature of the dissociation.[15,16] The vibrational source term S_V is the sum of the translational–vibrational energy exchanges (S_{T-V}) and the energy removal contribution due to vibration–chemistry coupling (S_{V-R}). The former are modeled according to Landau–Teller theory[16]:

$$S_{T-V} = \sum_m \rho_m \frac{e_{m_V}(T) - e_{m_V}(T_V)}{\tau_m} \tag{6}$$

where the vibrational relaxation time τ_m is defined as the sum of the molar-averaged Millikan–White[17] relaxation time and the collision-limited time, as described in Ref. 15. The energy removal contribution is defined according to Refs. 15 and 18, that is,

$$S_{V-R} = \sum_m \omega_m e_{m_V} \tag{7}$$

The closure of the equations is obtained by a gradient-law assumption and the use of a linear two-equation K–ε eddy viscosity model. Note that in the presence of chemical reactions such a gradient-law assumption has been shown to give unphysical results, at least in the case of premixed turbulent flames[19] (where counterdiffusion was observed). However, we argue that under hypersonic conditions such a phenomenon should be precluded due to the strong directionality of the flow; hence, the constitutive equations for the turbulent diffusion contributions are

$$-\bar{\rho}\widetilde{u_j'' Y_k''} = \frac{\mu^t}{Sc_k^t}\frac{\partial \tilde{Y}_k}{\partial x_j}, \qquad -\bar{\rho}\widetilde{u_i'' u_j''} = 2\mu^t \bar{S}_{ij} - \frac{2}{3}\left(\mu^t \bar{S}_{ll} + \bar{\rho}K\right)\delta_{ij}$$

$$-\bar{\rho}\widetilde{u_j'' e_T''} = c_{pT}\frac{\mu^t}{Pr_T^t}\frac{\partial \tilde{T}}{\partial x_j}, \qquad -\bar{\rho}\widetilde{u_j'' e_V''} = c_{pV}\frac{\mu^t}{Pr_V^t}\frac{\partial \tilde{T}_V}{\partial x_j} \tag{8}$$

where μ^t, Pr_T^t, Pr_V^t, and Sc_k^t are, respectively, the turbulent mixture viscosity, the turbulent Prandtl number for translational–rotational and vibrational heat conductions, and the turbulent Schmidt number of species k. In particular, $Pr_T^t = \sigma_T$ and $Pr_V^t = Pr_T^t\,(c_{pV}\eta_T)/(c_{pT}\eta_V)$; as in the case of turbulent compressible flows of ideal gases, we have assumed a value of $\sigma_T = 0.9$ and, in addition, we have set a unit species turbulent Schmidt number.

The turbulent mixture viscosity is defined in terms of the turbulent kinetic energy and the (isotropic) dissipation rate ε (Ref. 20), that is,

$$\mu^t = C_\mu f_\mu \bar{\rho}\ell_m K^{\frac{1}{2}}, \qquad \ell_m = \min\left[2.25\, y, \left(K^{\frac{3}{2}}/\varepsilon\right)\right] \tag{9}$$

where $C_\mu = 0.09$ and f_μ is a near-wall damping function given by

$$f_\mu = \left(1 + 3.45\Big/\sqrt{Re_t}\right)\tanh(y^+/80)$$

$$Re_t = \bar{\rho}K^2/\varepsilon\mu, \qquad y^+ = \bar{\rho}y(u_\tau/\mu) \tag{10}$$

and y and u_τ are, respectively, the distance normal to the wall and the friction velocity. The modeled transport equations for K and ε are

$$\frac{\partial \bar{\rho}K}{\partial t} + \frac{\partial \bar{\rho}\tilde{u}_j K}{\partial x_j} = \frac{\partial}{\partial x_j}\left[\left(\mu + \frac{\mu^t}{\sigma_K}\right)\frac{\partial K}{\partial x_j}\right] + P_K - \bar{\rho}\varepsilon + \Pi_c \tag{11}$$

$$\frac{\partial \bar{\rho}\varepsilon}{\partial t} + \frac{\partial \bar{\rho}\tilde{u}_j \varepsilon}{\partial x_j} = \frac{\partial}{\partial x_j}\left[\left(\mu + \frac{\mu^t}{\sigma_\varepsilon}\right)\frac{\partial \varepsilon}{\partial x_j}\right] + (C_{\varepsilon_1} P_K - C_{\varepsilon_2} f_2\, \varepsilon)\frac{\varepsilon}{K} \tag{12}$$

with

$$f_2 = [1 - \exp(-y^+/4.9)]^2 \tag{13}$$

$$C_{\varepsilon_1} = 1.83 - \left(k_v^2 \Big/ \sigma_\varepsilon \sqrt{C_\mu}\right);$$

$$C_{\varepsilon 2} = 1.83\left[1 - \tfrac{2}{9}\exp\left(-Re_t^2/36\right)\right] \tag{14}$$

and $k_v = 0.37$, $\sigma_K = 1.55$, and $\sigma_\varepsilon = 2$ (Ref. 20). The turbulent kinetic energy production contributions, respectively, due to mean velocity gradients and compressibility effects are

$$P_K = \left[2\mu^t\left(\bar{S}_{ij} - \frac{1}{3}\bar{S}_{ll}\delta_{ij}\right) - \frac{2}{3}\bar{\rho}K\delta_{ij}\right]\bar{S}_{ij} \tag{15}$$

$$\Pi_c = (-0.4P_K + 0.2\bar{\rho}\varepsilon)M_t^2 - \frac{\mu^t}{\bar{\rho}^2}\frac{1}{\sigma_\rho}\frac{\partial \bar{\rho}}{\partial x_j}\frac{\partial \bar{p}}{\partial x_j}$$

$$- 0.4\bar{\rho}\varepsilon\left\{1 - \exp\left[-\left(\frac{M_t - 0.3}{0.8}\right)^2\right]\right\} \tag{16}$$

where $M_t = \sqrt{[2K/(\gamma RT)]}$ and $\sigma_\rho = 0.5$.

Numerical Solution

The numerical solution of the governing equations for high-speed flows requires the use of robust and accurate schemes. The approach followed in the present work is based on a finite volume formulation of the equations that relies on a second-order, upwind-biased total variation diminishing discretization of the inviscid fluxes and central differencing of the viscous ones. (The details of the scheme for full nonequilibrium simulations are reported in Ref. 15.) Note that the transport equations for K and ε are loosely coupled with the mean flow equations; hence, their finite volume approximation is obtained by discretizing the convective fluxes following the approach of Larrouturou[21] for an approximate Riemann solver for a multicomponent gas. In the presence of turbulent nonequilibrium flows, stiffness arises due to disparity among the characteristic timescales of the relaxation processes and between the turbulent and fluid dynamic ones. For steady flows, stiffness can be reduced by preconditioning the system of discretized (ordinary differential) equations and defining the precondition matrix in terms of the partial Jacobian of the source terms. The time integration is then performed by a three-stage Runge–Kutta algorithm with a point-implicit treatment of the source terms.[15]

Results

To assess the capability of the model, we have first computed the flow around a cylinder flare configuration (test 1) that has been tested in the ONERA-F4 high-enthalpy wind tunnel. The model has then been applied to simulate shock-wave/turbulent boundary-layer interactions around a control surface configuration typical of a reusable launch vehicle (RLV) concept. The objective of the study has been to assess the effects of wall temperature, body-flap deflection and turbulence in the presence of thermal and chemical nonequilibrium, and their influence on the body-flap efficiency.

Test 1: Hollow Cylinder Flare

The axisymmetric cylinder flare geometry (see Fig. 1) is composed by a hollow cylinder with sharp leading edge, an external diameter of 0.15 m, and a length $L = 0.2$ m, followed by a 35-deg conical flare (whose length is 0.067 m) and an additional cylindrical extension, which is 0.033 m long, set to inhibit the effects of the base flow on the interaction region. To measure the pressure distribution the model is equipped with DRUCK FDCR-42 transducers; in particular, 22 pressure taps are located along an upper generating line. To check the correct position of the model inside the test chamber, the model is equipped with four additional control taps located symmetrically along the generating line at ±90 deg with respect to the original one. To measure the heat flux, the model is equipped with 22 thermocouples located on a generating line at 180 deg from the upper generating line and at the same streamwise positions (of the pressure taps). The accuracy of the

pressure and heat flux measurements is, respectively, ±5% and ±7%. ONERA-F4 high-enthalpy wind-tunnel flow conditions at the nozzle exit are close to equilibrium ($M_\infty = 9.4$, $Re_\infty/m = 1.115 \times 10^5$, $T_\infty = 522$ K, and $V_\infty = 4318$ m/s), thus corresponding to a stagnation pressure $p_0 = 230$ bar and a total enthalpy $H_0 = 9.93$ MJ/kg. The initial air composition in terms of molar fractions is $X_{O_2} = 0.2$ and $X_{N_2} = 0.8$, and the wall is assumed noncatalytic with fixed temperature $T_{wall} = 300$ K.

For this test case we have carried out four simulations assuming 1) laminar flow and ideal gas (T1.1), 2) laminar flow and nonequilibrium gas (T1.2), 3) turbulent flow and ideal gas (T1.3), and 4) turbulent flow and nonequilibrium gas (T1.4). For the turbulent simulations, the location of the laminar-to-turbulencetransition has been determined through the transition criterion derived from space shuttle flight data.[22] In particular, according to such criterion, transition is assumed to occur when the momentum thickness Reynolds number verifies the relation $Re_\theta/M_e = \mathcal{O}$ (100–200), where M_e is the Mach number at the edge of the laminar boundary layer whose properties have been determined through numerical simulations. For the conditions corresponding to test 1, the criterion indicates that transition occurs at $X_{tran}/L = 0.25$. As a compromise between accuracy and computational cost, all numerical simulations have been carried out on a grid consisting of 264 × 96 cells (see Fig. 1; the minimum nondimensional grid spacings in streamwise and normal-to-the-wall directions are, respectively, 0.52×10^{-3} and 0.53×10^{-4}) that has been selected through a grid sensitivity analysis both for laminar and turbulent conditions. The results of the grid sensitivity are reported in Fig. 2 in terms of separation location X_{sep}/L and peak Stanton number St_{peak} as a function of grid resolution (defined as the inverse of the square root of the total number of cells, N). Figure 2 shows

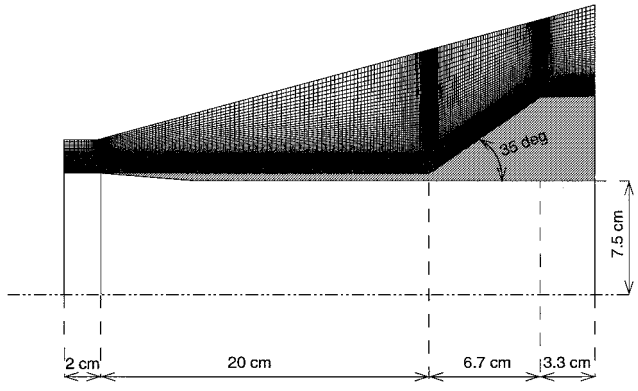

Fig. 1 Cylinder flare geometry and grid.

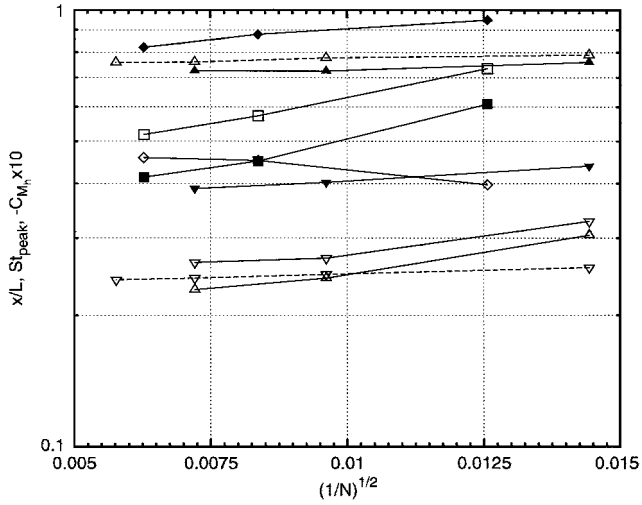

Fig. 2 Cylinder flare and RLV, grid sensitivity analysis: open symbols, laminar; filled symbols, turbulent. Test 1: □, X_{sep}/L; and ◇, St_{peak} × 10. Test 2 (——, $\delta = 30$ deg and - - - -, $\delta = 10$ deg): △, X_{sep}/L; and ▽, $-C_{M_h}$ × 10.

Table 1 Test 1 characteristic parameters

Test	X_{sep}, m	X_{rea}, m	$C_{p_{peak}}$	St_{peak}
T1.1	0.0966	0.2478	1.5438	0.04601
T1.2	0.1023	0.2465	1.5716	0.04585
T1.3	0.1079	0.2453	1.5817	0.05339
T1.4	0.1107	0.2439	1.5849	0.05361
Experiment (ONERA)	0.1245	0.2365	1.1226	0.07168

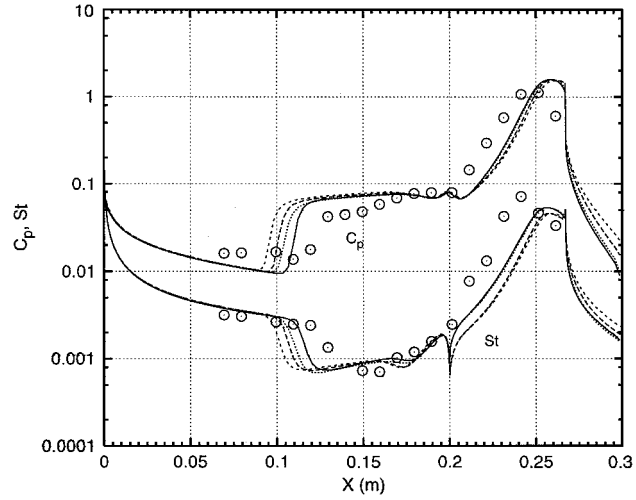

Fig. 3 Cylinder flare, surface distributions of pressure coefficient and Stanton number along the wall: - - - -, T1.1; – – –, T1.2; · · · ·, T1.3; ——, T1.4; and ○, experiment (ONERA).

that the laminar Stanton number peak is grid independent; however, the distributions of the separation location (either laminar or turbulent) and the turbulent Stanton number peak as a function of grid resolution indicate that a further grid refinement is necessary.

The results of the test cases T1.1–T1.4 are reported in Fig. 3 in terms of pressure coefficient and Stanton number distributions together with experimental measurements. Figure 3 (and Table 1) reveals that the upstream influence is reduced (with a delay in the separation) approximately by 3–5% due to nonequilibrium effects; likewise, turbulence reduces the upstream influence by a factor of approximately 10%. Figure 3 also shows that 1) the pressure plateau and the peak dynamic load are not significantly affected either by nonequilibrium or by turbulence, 2) turbulence is responsible for a faster pressure recovery and an increase in the heat transfer over the flare, and 3) the peak thermal load is primarily affected by turbulence (with an increase of approximately 16%). In addition, the turbulent nonequilibrium gas simulation yields an overestimation (with respect to the experiment) of the upstream influence by a factor of 18% and an underestimation of peak heating of about 30%.

Test 2: RLV

The primary goal of the study is to analyze the aerodynamic performance of the control surface of a RLV concept developed in the framework of the FESTIP program of ESA.[23] In particular, we have considered the FSSC-15-OAE suborbital hopper geometry that has a flat bottom. We recall that in Ref. 24 it was concluded that for such a configuration the flow exhibits a quasi-two-dimensional structure. In the present study, we have then considered the geometry corresponding to the symmetry plane of the hopper as shown in Fig. 4, which also reports all of the characteristic dimensions of the vehicle. Note that a flat extension has been added behind the flap to enforce supersonic outflow. The flow conditions of test 2 correspond to a reentry into the atmosphere at an altitude of 51.9 km and velocity $V_\infty = 3.28$ km/s (thus yielding freestream Mach and Reynolds numbers equal to, respectively, $M_\infty = 9.99$ and $Re_\infty/m = 1.578 \times 10^5$), at an angle of attack of 19.2 deg. From the flight-path analysis, at these conditions turbulence is expected to play a role. To assess the importance of turbulence, we have then carried out both laminar and turbulent simulations at various wall temperatures and body-flap deflections.

All computations have been performed on a 180×60 grid (see Fig. 4), whose minimum nondimensional spacings in streamwise and normal-to-the-wall directions are, respectively, 0.69×10^{-3} and 0.59×10^{-7}. The grid has been selected through a grid sensitivity analysis under laminar and turbulent flow conditions. The results of this study are reported in Fig. 2 in terms of separation location X_{sep}/L and hinge moment coefficient C_{M_h} (see a later section for its definition) at two values of the body-flap deflection ($\delta = 10$ and $\delta = 30$ deg). Figure 2 shows the grid convergence of results for both the laminar and turbulent conditions. The definitions of the test cases are reported in Table 2 in terms of flow conditions (laminar or turbulent), body-flap deflection angle, and wall temperature. Observe that most of the laminar computations have been performed with the assumption of surface radiation cooling, that is, the heat flux transfered from the gas to the wall is assumed to balance the heat flux radiated away from the surface. Hirschel[25] has shown that, in the hypothesis of zero heat flux into the wall, this mechanism yields a radiation-adiabatic equilibrium temperature $T_{\text{rad.eq.}}$ that is a good approximation of the temperature attained at the wall. For the turbulent simulations, the transition location has been determined by means of the same correlation formula used for test 1; in particular, we have assumed that transition occurs when $Re_\theta/M_e = \mathcal{O}$ (100–200), where the laminar boundary-layer properties have been determined numerically. For the conditions of the test, the criterion indicates that laminar-to-turbulence transition occurs approximately at one-third of the body length ($X_{\text{tran}}/L = 0.365$ from the nose).

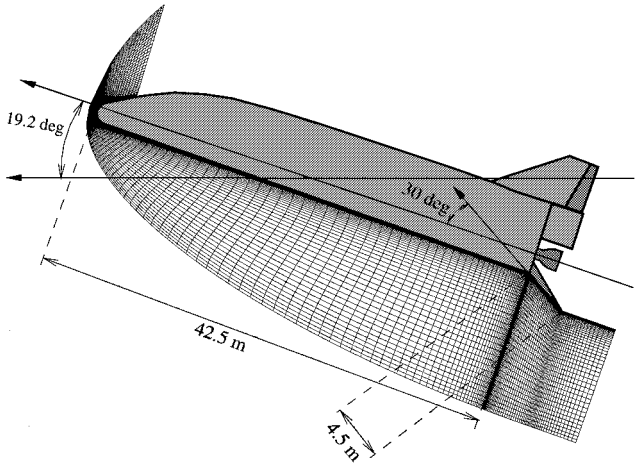

Fig. 4 RLV geometry and grid ($\delta = 30$ deg).

In Fig. 5 we show the Mach number contour lines (with a zoom of the body-flap region) for the conditions corresponding to a body-flap deflection $\delta = 30$ deg and turbulent flow assumption. The flowfield exhibits a detached bow shock ahead of the nose with a stagnation region characterized by air dissociation and high surface heat transfer rates. The strong bow shock curvature around the nose produces an entropy layer (as inferred from the Mach number gradients in the direction normal to the wall, see Fig. 5) that is swallowed by the boundary layer that develops along the body and that controls the shock-wave/boundary-layer interaction around the body flap. Observe that, due to the shape of the vehicle and the flat extension of the body flap, the flow reattaches at the flap trailing edge. The flow exhibits a moderate air dissociation within the shock layer ($Y_{\text{O}} \simeq 0.09$ and $Y_{\text{NO}} \simeq 0.07$ along the stagnation streamline); in addition, an analysis (not reported) of the vibrational and translational temperature distributions along the stagnation line shows that thermal equilibrium is obtained on a scale $\mathcal{O}$ (2%) of the nose radius.

In Figs. 6 and 7, we report the distributions of the pressure coefficient and Stanton number for laminar (both for the radiation equilibrium and the fixed wall temperature $T_{\text{wall}} = 800$ K) and turbulent conditions (at various wall temperatures, $T_{\text{wall}} = 300$, 500, 800, and 1000 K) along the body surface at a given body-flap deflection ($\delta = 30$ deg). In Fig. 6 we also show the pressure coefficient distribution determined by means of the blast wave theory with the Newtonian correction to account for the effects of the angle of attack.[26]

Table 2 Test cases definitions: physical model, flap deflection, and wall temperature

δ, deg	Laminar flow	Turbulent flow
5	$T_{\text{wall}} = T_{\text{rad.eq.}}$	$T_{\text{wall}} = 800$ K
10	$T_{\text{wall}} = T_{\text{rad.eq.}}$	——
15	$T_{\text{wall}} = T_{\text{rad.eq.}}$	$T_{\text{wall}} = 800$ K
20	$T_{\text{wall}} = T_{\text{rad.eq.}}$	——
25	$T_{\text{wall}} = T_{\text{rad.eq.}}$	$T_{\text{wall}} = 800$ K
30	$T_{\text{wall}} = T_{\text{rad.eq.}}$, 300, 500, 800 K	$T_{\text{wall}} = 300$, 500, 800, 1000 K

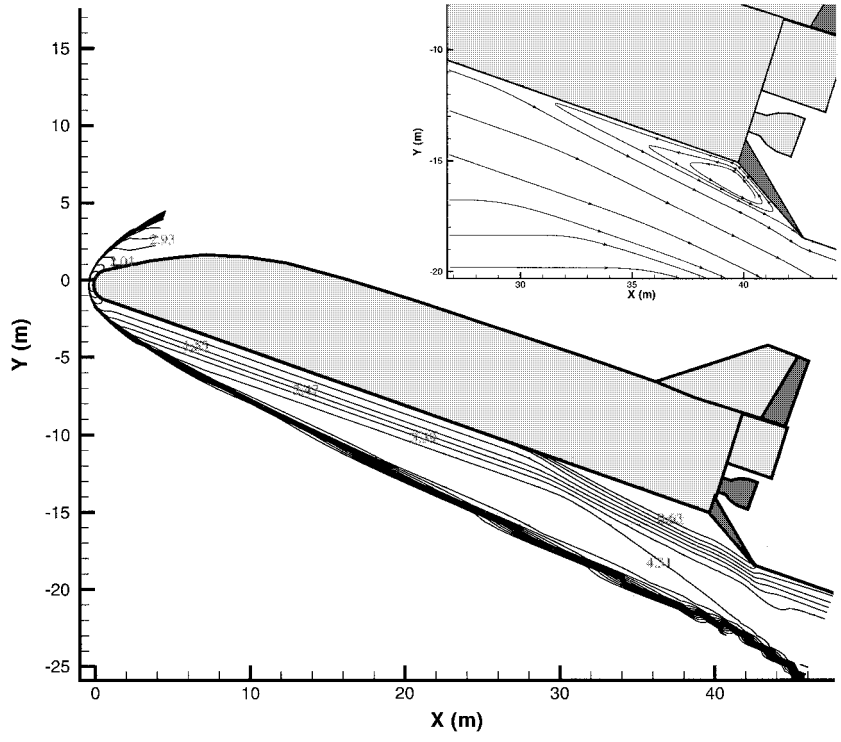

Fig. 5 RLV Mach number contours and zoom of the streamlines around the hingeline ($\delta = 30$ deg and $T_{\text{wall}} = 800$ K).

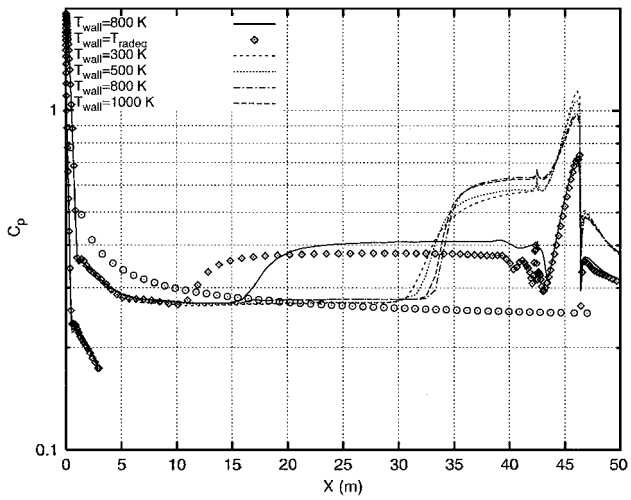

Fig. 6 RLV surface distributions of pressure coefficient at $\delta = 30$ deg: ——, laminar; ◇, laminar with surface radiation cooling; - - - -, turbulent; and ○, blast-wave theory with Newtonian correction.

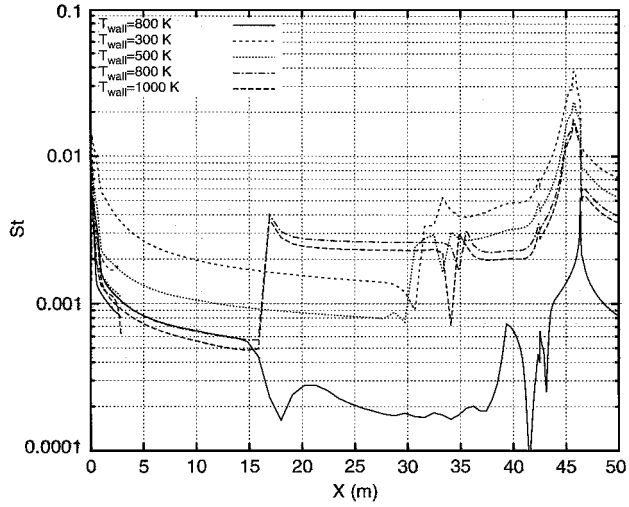

Fig. 7 RLV surface distributions of Stanton number at $\delta = 30$ deg: ——, laminar and - - - -, turbulent.

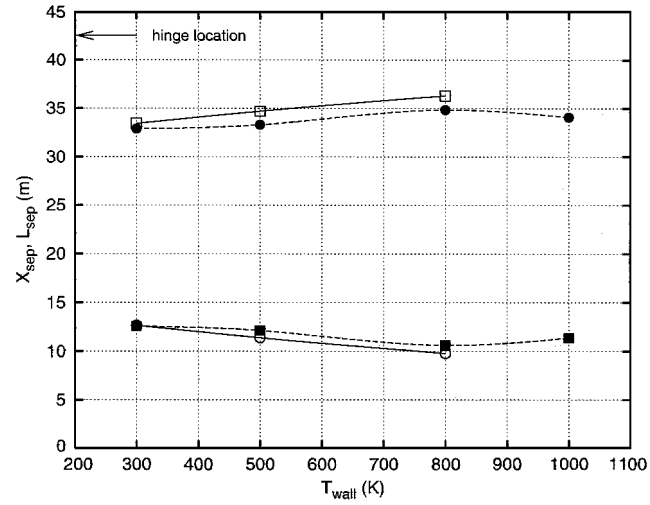

Fig. 8 RLV location X_{sep} and extent L_{sep} of separation as a function of wall temperature at $\delta = 30$ deg (open symbols, laminar and filled symbols, turbulent): □, L_{sep} and ○, X_{sep}.

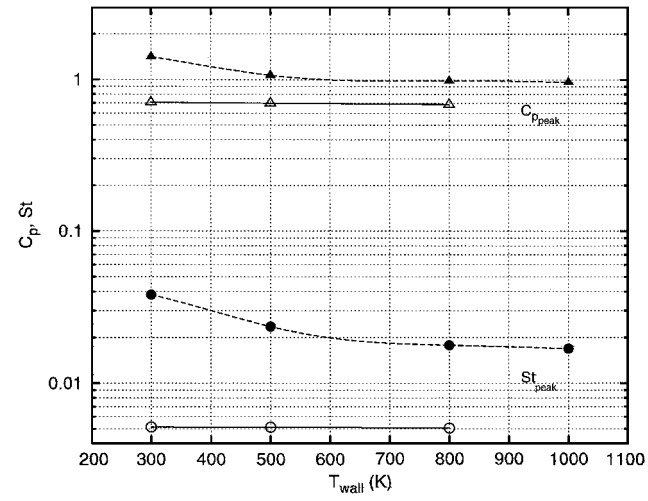

Fig. 9 RLV distributions of the peak pressure coefficient $C_{p_{peak}}$ and peak Stanton number St_{peak} as a function of wall temperature at $\delta = 30$ deg (open symbols, laminar and filled symbols, turbulent: △, $C_{p_{peak}}$ and ○, St_{peak}.

The comparison suggests that the pressure level attained ahead of the interaction is mainly controlled by the incidence. Figure 6 indicates that, if one assumes surface radiation cooling (under laminar conditions) the wall temperature along the forebody is (locally) higher than in the case of constant value. As a consequence, the boundary layer is thicker, the separation is anticipated, the upstream influence is larger, and the plateau pressure is lower; however, the pressure recovery over the flap is only slightly affected. The observation is very important for the extrapolation-to-flight of wind-tunnel measurements because it is generally impossible to reproduce the actual surface temperature distribution in wind-tunnel experiments. Figure 6 shows that laminar simulations predict a separation larger than in the case of turbulent conditions and a multiple-vortex structure with the occurrence of local stagnations and subsequent peak heatings (see Fig. 7). The sudden increase in the Stanton number at a location that depends on the wall temperature clearly indicates that the shock-wave/boundary-layer interaction around the body flap is indeed turbulent. The strong flow expansion at the flap trailing edge is due to the presence of the flat extension that fixes the reattachment point.

Effects of Wall Temperature

Figures 6 and 7 show that for lower temperatures ($T_{wall} = 300$ and 500 K), even though laminar-to-turbulence transition is fixed at $X_{tran}/L = 0.365$, turbulence effects are significant only downstream of the separation shock, which acts as a turbulence amplification mechanism. Hence, the upstream influence is larger, thus causing a greater loss of flap pressure recovery (Fig. 6). At higher temperatures ($T_{wall} = 800$ and 1000 K) turbulence is active at approximately one-third of the vehicle's length, that is, downstream of the location where laminar-to-turbulence transition is assumed to occur. Figure 7 then suggests that laminar-to-turbulence transition is delayed due to wall cooling, thus having a stabilizing effect on turbulence (as also shown in Ref. 22). Consequently, because of boundary-layer thinning, the values of Stanton number over the flap increase. In Fig. 8, the location of separation X_{sep} and its extent L_{sep} are reported as a function of the wall temperature both for laminar and turbulent conditions. The results show a nearly linear increase of L_{sep} with T_{wall} for the laminar case; for turbulent conditions L_{sep} exhibits a nearly linear decrease up to $T_{wall} = 800$ K, then a reversal trend is observed for $T_{wall} > 800$ K. Figure 9 shows the peak values of the pressure coefficient and Stanton number over the flap. Figure 9 shows that under turbulent conditions the aerothermal loads decrease with increasing T_{wall} (due to the effects of wall temperature on laminar-to-turbulence transition and boundary-layer thickening), whereas negligible variations of peak loads are predicted under laminar conditions.

Effects of Body-Flap Deflection

The effects of body-flap deflection angle are shown in Figs. 10 and 11, where the pressure coefficient and the Stanton number

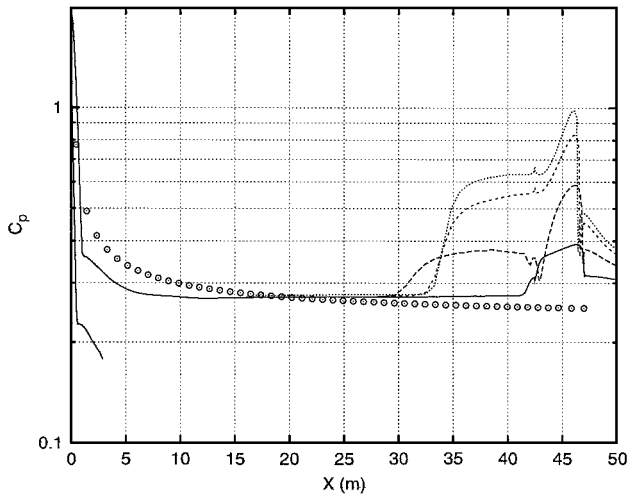

Fig. 10 RLV surface distributions of pressure coefficient at various body-flap angles δ at T_{wall} = 800 K: ——, δ = 5 deg; – – –, δ = 15 deg; - - -, δ = 25 deg; and · · · ·, δ = 30 deg; ○, blast-wave theory with Newtonian correction.

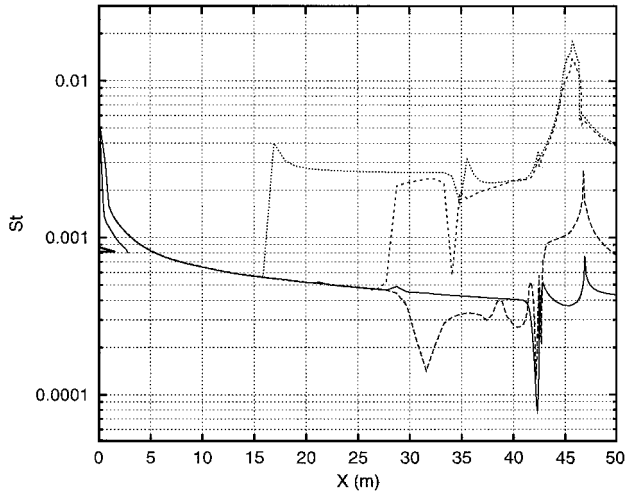

Fig. 11 RLV surface distributions of Stanton number at various body-flap angles δ at T_{wall} = 800 K: ——, δ = 5 deg; – – –, δ = 15 deg; - - -, δ = 25 deg; and · · · ·, δ = 30 deg.

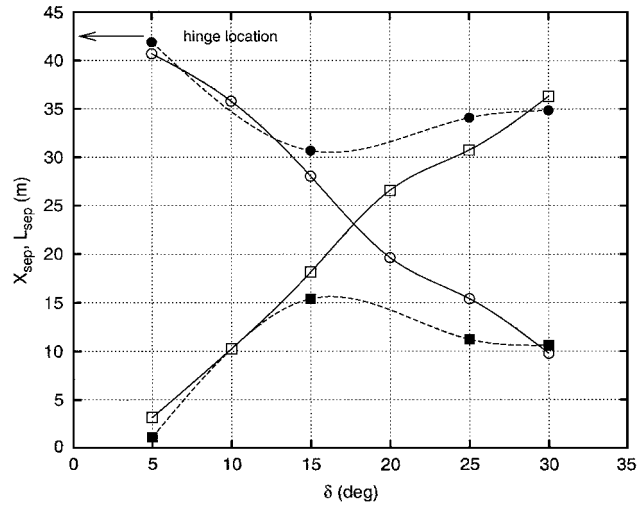

Fig. 12 RLV location X_{sep} and extent L_{sep} of separation as a function of body-flap angle δ (open symbols, laminar conditions and filled symbols, turbulent conditions with T_{wall} = 800 K): □, L_{sep} and ○, X_{sep}.

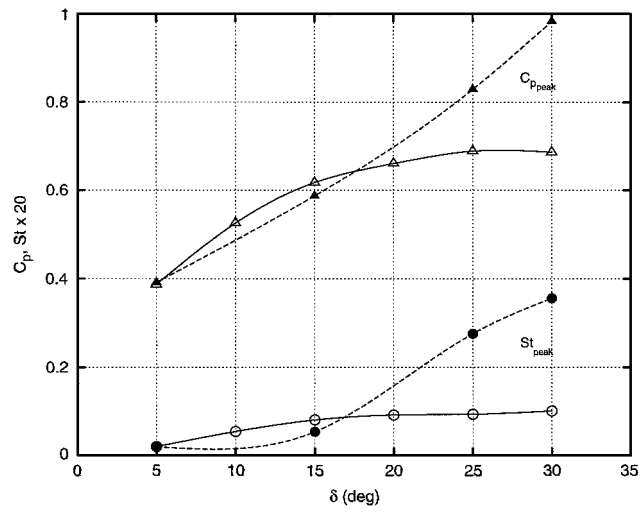

Fig. 13 RLV distributions of the peak pressure coefficient $C_{p_{peak}}$ and peak Stanton number St_{peak} as a function of body-flap angle δ (open symbols, laminar conditions and filled symbols, turbulent conditions with T_{wall} = 800 K): △, $C_{p_{peak}}$ and ○, St_{peak}.

distributions are plotted for various δ at a given wall temperature ($T_{wall} = 800$ K). The levels of the plateau pressure and the pressure recovery on the flap increase with δ (Fig.10); the upstream influence increases up to $\delta = 15$ deg, and then it decreases for greater δ. Laminar shock-wave/boundary-layer interactions are predicted around the flap for $\delta = 5$ and 15 deg. At higher body-flap deflections, turbulence is active ahead of the separation shock (at a location $X_{tran} \simeq 27.5$ m for $\delta = 25$ deg and $X_{tran} \simeq 15.5$ m for $\delta = 30$ deg; see Fig. 11). As a consequence, the interaction occurs under fully turbulent conditions, and the peak Stanton number is increased approximately by one order of magnitude (Fig. 11). Figure 12 shows that under laminar conditions both the extent of separation L_{sep} and its location X_{sep} vary approximately linearly with δ. For turbulent simulations, the results indicate that X_{sep} and L_{sep} exhibit a change of behavior for $\delta \geq 15$ deg. This is more clearly observed in Fig. 13, which shows that turbulence effects on pressure and thermal loads become important for flap deflections greater than 15 deg. Indeed, for $\delta \geq 15$ deg, the separation shock is strong enough to activate turbulence, and the distributions of the peak pressure coefficient and Stanton number show a clear bifurcation at this critical body-flap angle.

Separation and Plateau Pressure Correlation Law

For shock-wave/boundary-layer interactions over compression ramps,[4–6] the separation and plateau pressure coefficients ($C_{p_{sep}}$ and $C_{p_{pla}}$) correlate well with the Mach and Reynolds numbers (M_0 and Re_{x_0}) evaluated at a location immediately upstream of the interaction ($x = x_0$) according to

$$C_{p_{sep/pla}} = K_{sep/pla}\left[\left(M_0^2 - 1\right) Re_{x_0}\right]^{-\frac{1}{4}} \tag{17}$$

where $K_{sep/pla}$ is a constant determined through comparison with experiments. For an RLV at incidence, we argue that the same type of dependency on M_0 and Re_{x_0} holds, provided the Newtonian pressure contribution due to the incidence α is accounted for,[26] and Eq. (17) is modified accordingly, thus yielding

$$C_{p_{sep/pla}} = K_{sep/pla}\left[\left(M_0^2 - 1\right) Re_{x_0}\right]^{-\frac{1}{4}} + 2\sin^2\alpha \tag{18}$$

Hence, to better understand the effects of flap angle, wall temperature, and turbulence, in Fig. 14 we show all of the computed separation and plateau pressure coefficients as a function of the scaling parameter $[(M_0^2 - 1)\ Re_{x_0}]^{-1/4}$. For laminar conditions we also report the correlations corresponding to Eq. (18), where we have used $K_{sep} = 4.1$ and $K_{pla} = 6.6$ (determined through a least-square fit). Figure 14 shows that laminar results well correlate with Eq. (18), even when accounting for real gas effects. With regard to the turbulent simulations, we observe that at a given wall temperature

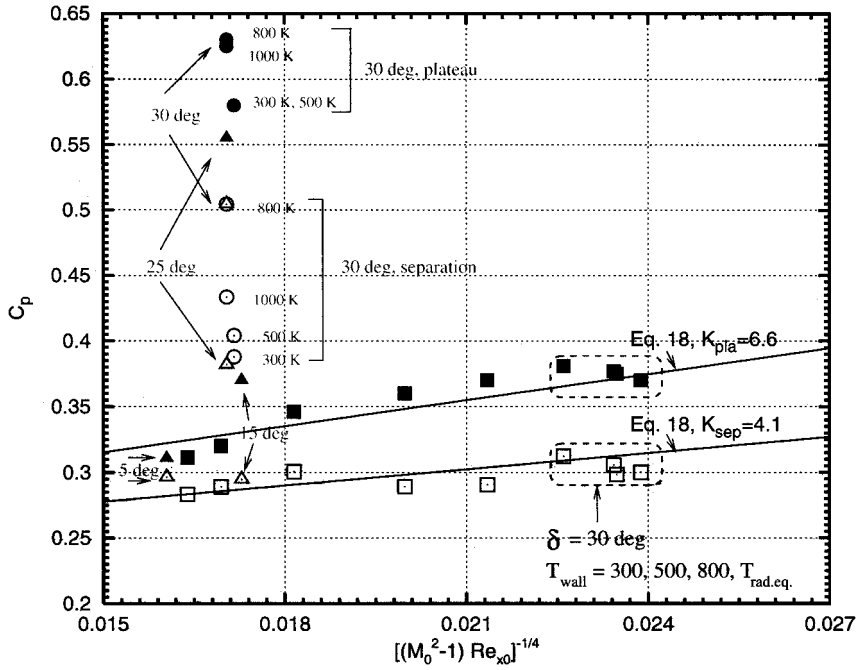

Fig. 14 RLV distributions of separation and plateau pressure coefficients ($C_{p_{sep}}$ and $C_{p_{pla}}$) in function of $[(M_0^2 - 1)\,Re_{x_0}]^{-1/4}$ (open symbols, values at separation and filled symbols, plateau values). Influence of T_{wall}: □, laminar conditions and ○, turbulent conditions. Influence of δ: □, laminar conditions and △, turbulent conditions.

($T_{wall} = 800$ K) separation is laminar up to $\delta = 15$ deg, and then turbulence plays a role and the values of $C_{p_{sep}}$ and $C_{p_{pla}}$ strongly increase with δ. For the largest flap deflection ($\delta = 30$ deg) turbulence is active immediately ahead of separation for values of $T_{wall} = 300$ and 500 K; at higher wall temperatures ($T_{wall} = 800$ and 1000 K) turbulence is active downstream of the location where transition is assumed to occur. However, in both cases the interaction occurs again under fully turbulent conditions, and the computed values of $C_{p_{sep}}$ and $C_{p_{pla}}$ are greater than the laminar correlation corresponding to Eq. (18).

Considerations on Flap Efficiency

The aerodynamic performance of the FSSC-15-OAE body flap is analyzed in terms of flap efficiency and flap operating envelope, and the results are plotted in Figs. 15 and 16. The flap efficiency E_{flap} is defined in terms of pitching moment coefficient C_{M_h} as

$$E_{flap} = C_{M_h}(\delta) - C_{M_h}(0),$$

$$C_{M_h} = \frac{2\int_{x_{bf}}^{x_{ef}} (-p\boldsymbol{n} + \boldsymbol{\tau}) \cdot (\boldsymbol{x} - \boldsymbol{x}_h)\,\mathrm{d}s}{\rho_\infty V_\infty^2 S_{ref} L_{flap}} \tag{19}$$

where $S_{ref} = 47$ m, $L_{flap} = x_{ef} - x_{bf} = 4.5$ m, and $C_{M_h}(0) = -1.5072 \times 10^{-2}$ is the pitching moment computed on the clean configuration (undeflected flap, $\delta = 0$ deg). The value of C_{M_h} depends on the pressure (and shear stress) distribution over the flap surface, thus being strongly affected by the presence of a shock-wave/boundary-layer interaction around the hinge. (Note that a negative C_{M_h} acts to reduce the angle of attack.) Hence, flap efficiency gives a clear idea of the response mechanism to a variation of the body-flap angle. Recall that, to an increase of δ, if the pressure recovery on the ramp does not balance the contribution of the pressure plateau, the shock-wave/boundary-layer interaction yields a loss in control effectiveness. Vice versa, if the flap overpressure (due to the increase of δ) inhibits the deteriorating effects of flow separation, then the shock-wave/boundary-layer interaction has a beneficial effect on the control effectiveness of the flap.

The distribution of flap efficiency as a function of flap deflection is shown in Fig. 15, where we show both laminar and turbulent results. For the latter condition, Fig. 15 confirms the bifurcation in the behavior at the value $\delta \approx 15$ deg. For $\delta < 15$ deg, the shock-wave/boundary-layer interaction around the hinge is certainly laminar; indeed, the separation shock is rather weak and does not cause any significant turbulence amplification. A clear loss of flap efficiency is predicted under laminar conditions for $\delta > 15$ deg; however, when turbulence effects become important (i.e., when the separation shock is strong enough to promote transition) an improvement of flap efficiency is observed. At the largest flap deflection ($\delta = 30$ deg) turbulent conditions yield a flap efficiency about twice the corresponding laminar value. The explanation for this behavior is that for turbulent conditions the thickness of the subsonic portion of the boundary layer (across which pressure disturbances propagate upstream) is thinner, thus producing a smaller separation and, consequently, a greater pressure recovery on the flap. A reduction of flap efficiency with increasing T_{wall} due to the progressive loss of pressure recovery on the flap is also shown in Fig. 15 for $\delta = 30$ deg. As already observed in Ref. 27, under laminar conditions wall temperature does not affect significantly the flap efficiency, whereas a significant dependency is observed for turbulent flow conditions (a 16% larger flap efficiency is predicted for $T_{wall} = 300$ K with respect to the value corresponding to $T_{wall} = 1000$ K). Figure 16 shows the

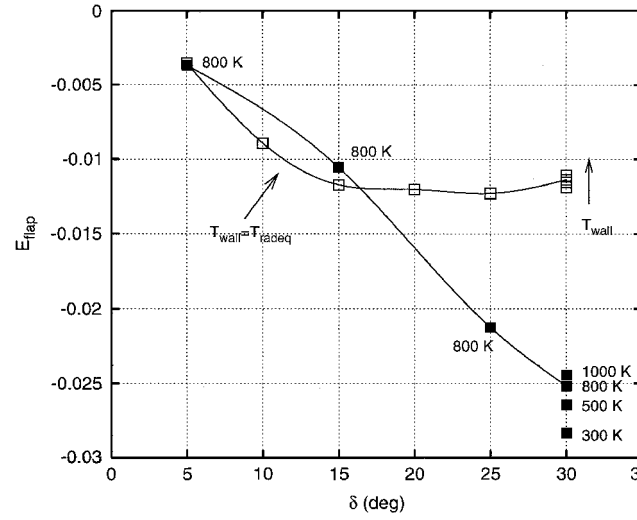

Fig. 15 RLV body-flap efficiency E_{flap} as a function of body-flap angle δ at various wall temperatures: □, laminar conditions and ■, turbulent conditions.

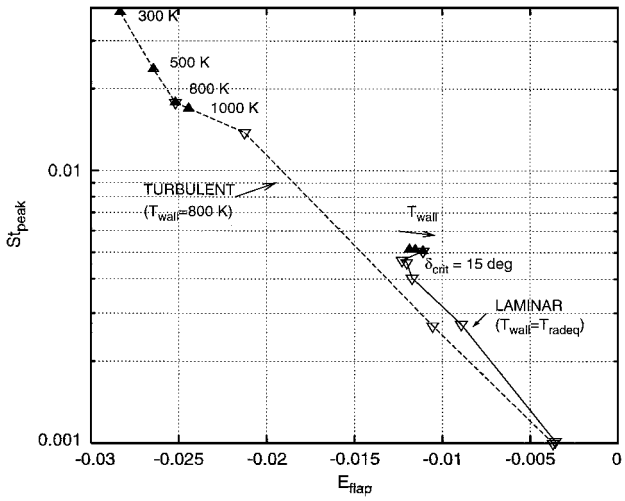

Fig. 16 RLV body-flap operating envelope. Distribution of the peak Stanton number St_{peak} as a function of body-flap efficiency at various δ and T_{wall} (——, laminar and - - - -, turbulent): open symbols, influence of δ and filled symbols, influence of T_{wall}.

flap operating envelope, that is, the distribution of the peak Stanton number as a function of flap efficiency at various δ and T_{wall}. Figure 16 shows that for laminar conditions there exists a critical flap deflection $\delta_{crit} \approx 15$ deg: For $\delta < \delta_{crit}$, both flap efficiency and flap heating increase, whereas for $\delta > \delta_{crit}$, a clear loss of performance with a nearly constant flap heating is observed. This suggests that for laminar flow conditions one should operate the body flap only up to δ_{crit} (at most). However, from the simulations, we conclude that turbulence effects become important just around δ_{crit}, thus extending the operating capabilities of the aerodynamic control surface up to $\delta = 30$ deg, provided a proper thermal protection system is mounted over the flap. Furthermore, a remarkable effect of wall temperature is observed for turbulent conditions (at $\delta = 30$ deg).

Conclusions

In the present work we have studied the influence of turbulence on shock-wave/boundary-layer interactions in the presence of thermal and chemical nonequilibrium phenomena. The numerical methodology employed is based on a finite volume, total variation diminishing approach with a point-implicit treatment of source terms and a linear eddy viscosity two-equation turbulence modeling that accounts for the coupling of turbulence with thermal and chemical nonequilibrium phenomena through properly defined turbulent Prandtl numbers.

The capabilities of the model have first been assessed by computing the flow around a cylinder flare configuration with a comparison with experimental measurements. The simulations indicate that for the selected test case the peak dynamic load and the plateau pressure are rather unaffected either by nonequilibrium or by turbulence effects. However, separation and thermal load are influenced both by turbulence and relaxation phenomena (the latter yielding a weaker influence).

The model has then been applied to analyze the flow around the body flap of an RLV. In particular, we have focused our attention on the effects of wall temperature and flap deflection on separation and on the aerothermal loads acting on the flap and its aerodynamic efficiency. The computed flowfields exhibit a detached bow shock around the vehicle, the formation of an entropy layer that is swallowed by the boundary layer on the forebody and a supersonic shock-wave/boundary-layer interaction around the body flap. For laminar conditions, the simulations show that an increase of the wall temperature causes an early separation with a nearly linear growth of the upstream influence and a progressively greater loss of flap efficiency. Surface radiation cooling produces a thickening of the boundary layer and a reduction of the plateau pressure and, consequently, the upstream influence increases. The turbulent simulations show that wall cooling delays laminar-to-turbulence transition: In particular, at low temperatures, turbulence is activated immediately ahead of the separation shock; the location at which turbulence is active is displaced upstream (and separation is delayed) as the wall temperature increases. Under laminar conditions, an increase of the body-flap deflection produces an increase both in the pressure recovery and peak thermal load along the flap; in addition, the extent of separation exhibits a nearly linear dependency on δ. With regard to the flap operating envelope, we conclude that both the flap efficiency and the flap heating increase with δ up to δ_{crit} ($\simeq$15 deg). For values of $\delta \geq \delta_{crit}$, the flap exhibits a clear loss of performance with a nearly constant flap heating. As in the case of ideal gas, the laminar simulations also show that dynamic loads, that is, separation and plateau pressures, well correlate with Mach and Reynolds numbers immediately upstream of the interaction. The effects of turbulence on aerothermal loads become important for values greater than 15 deg, and the interaction occurs under fully turbulent conditions. In addition, turbulence extends the operating capabilities of the aerodynamic control surface. The study also shows that the efficiency and the operating envelope of the body flap are significantly affected by the wall temperature only when turbulence is active.

Acknowledgment

This work was partially supported by the Italian Space Agency.

References

[1]Hirschel, E. H., "Aerothermodynamic Phenomena and the Design of Atmospheric Hypersonic Airplanes," *Advances in Hypersonics*, Defining the Hypersonic Environment, Vol. 1, Birkhäuser, Boston, 1992, pp. 1–39.

[2]Needham, D. A., and Stollery, J. L., "Boundary-Layer Separation in Hypersonic Flow," AIAA Paper 66-455, 1966.

[3]Holden, M. S., "Two-Dimensional Shock Wave–Boundary Layer Interactions in High Speed Flows. Part II, Experimental Studies on Shock Wave–Boundary Layer Interaction," AGARDograph AG-203, June 1975, pp. 41–110.

[4]Delery, J. M., "Shock Interference Phenomena in Hypersonic Flows," Third Joint Europe/U.S. Short Course in Hypersonics, Univ. of Aachen, Aachen, Germany, Oct. 1990.

[5]Grasso, F., and Marini, M., "Analysis of Hypersonic Shock Wave Laminar Boundary Layer Interaction Phenomena," *Computers and Fluids*, Vol. 25, No. 6, 1996, pp. 561–581.

[6]Grasso, F., Leone, G., and Delery, J. M., "Validation Procedure for the Analysis of Shock-Wave/Boundary-Layer Interaction Problems," *AIAA Journal*, Vol. 32, No. 9, 1994, pp. 1820–1827.

[7]Grasso, F., and Leone, G., "Chemistry Effects in Shock Wave Boundary Layer Interaction Problems," *Proceedings of the IUTAM Symposium on Aerothermochemistry of Spacecraft and Associated Hypersonic Flows*, Jouve, Paris, 1992, pp. 220–227.

[8]Mallinson, S. G., Gai, S. L., and Mudford, N. R., "The Interaction of a Shock Wave with a Laminar Boundary Layer at a Compression Corner in High-Enthalpy Flows Including Real Gas Effects," *Journal of Fluid Mechanics*, Vol. 342, 1997, pp. 1–35.

[9]Mallinson, S. G., Gai, S. L., and Mudford, N. R., "High-Enthalpy, Hypersonic Compression Corner Flow," *AIAA Journal*, Vol. 34, No. 6, 1996, pp. 1130–1137.

[10]Krek, R., Beck, W., and Eitelberg, G., "Hyperboloid Flare Experiments in the HEG," *Proceedings of the 20th International Symposium on Shock Waves*, World Scientific, Singapore, 1996.

[11]Davis, J. P., "Further Tests on the HALIS Axisymmetric Configuration in the T5 Hypervelocity Shock Tunnel," Graduate Aeronautical Lab., GALCIT TR FM 96-2, California Inst. of Technology, Pasadena, CA, 1996.

[12]Furumoto, G. H., Zhong, X., and Skiba, J. C., "Numerical Studies of Real-Gas Effects on Two-Dimensional Hypersonic Shock-Wave/Boundary-Layer Interaction," *Physics of Fluids*, Vol. 9, No. 1, 1997, pp. 191–210.

[13]Davis, J. P., and Sturtevant, B., "Separation Length in High-Enthalpy Shock/Boundary Layer Interaction," *Physics of Fluids*, Vol. 12, No. 10, 2000, pp. 2661–2687.

[14]Gupta, R. N., Yos, J. M., Thompson, R. A., and Lee, K. P., "A Review of Reaction Rates and Thermodynamic and Transport Properties for an 11-Species Air Model for Chemical and Thermal Nonequilibrium Calculations to 30,000 K," NASA RP 1232, Aug. 1990.

[15]Grasso, F., and Capano, G., "Modeling of Ionizing Hypersonic Flows in Nonequilibrium," *Journal of Spacecraft and Rockets*, Vol. 32, No. 2, 1995, pp. 217–224.

[16]Park, C., *Nonequilibrium Hypersonic Aerothermodynamics*, Wiley, New York, 1990, pp. 43–143.

[17]Millikan, R. C., and White, D. R., "Systematics of Vibrational Relaxation," *Journal of Chemical Physics*, Vol. 39, No. 12, 1963, pp. 3209–3213.

[18]Gnoffo, P. A., and Gupta, R. N., "Conservation Equations and Physical Models for Hypersonic Air Flows in Thermal and Chemical Nonequilibrium," NASA TP 2867, 1989.

[19]Libby, P. A., and Bray, K. N. C., "Countergradient Diffusion in Premixed Turbulent Flames," *AIAA Journal*, Vol. 19, No. 2, 1981, pp. 205–213.

[20]Grasso, F., and Falconi, D., "High-Speed Turbulence Modeling of Shock-Wave/Boundary-Layer Interaction," *AIAA Journal*, Vol. 31, No. 7, 1993, pp. 1199–1206.

[21]Larrouturou, B., "How to Preserve the Mass Fractions Positivity when Computing Compressible Multi-Component Flows," *Journal of Computational Physics*, Vol. 95, No. 1, 1991, pp. 59–84.

[22]Stetson, K. F., "Hypersonic Boundary-Layer Transition," *Advances in Hypersonics, Defining the Hypersonic Environment*, Vol. 1, Birkhäuser, Boston, 1992, pp. 324–417.

[23]Dujarric, C., "Proposed Orientations for Future European Launchers Concepts and Associated Aerothermodynamics Technology Development Requirements," *Proceedings of the Third European Symposium on Aerothermodynamics for Space Vehicles*, SP-426, ESA, Noordwijk, The Netherlands, 1998.

[24]Longo, J. M. A., and Radespiel, R., "Flap Efficiency and Heating of a Winged Re-Entry Vehicle," *Journal of Spacecraft and Rockets*, Vol. 33, No. 2, 1996, pp. 178–184.

[25]Hirschel, E. H., "Thermal Surface Effects in Aerothermodynamics," *Proceedings of the Third European Symposium on Aerothermodynamics for Space Vehicles*, SP-426, ESA, Noordwijk, The Netherlands, 1998.

[26]Anderson, J. D., Jr., *Hypersonic and High Temperature Gas Dynamics*, McGraw–Hill, New York, 1989, pp. 137, 138.

[27]Marini, M., "Effects of Flow and Geometry Parameters on Shock-Wave/Boundary-Layer Interaction Phenomena," AIAA Paper 98-1570, 1998.

M. Sichel
Associate Editor